Laser-driven 1 GeV carbon ions from preheated diamond targets in the break-out afterburner regime

Jung, D., Yin, L., Gautier, D. C., Wu, H-C., Letzring, S., Dromey, B., Shah, R., Palaniyappan, S., Shimada, T., Johnson, R. P., Schreiber, J., Habs, D., Fernández, J. C., Hegelich, B. M., & Albright, B. J. (2013). Laser-driven 1 GeV carbon ions from preheated diamond targets in the break-out afterburner regime. *Physics of Plasmas*, *20*(8), 083103. https://doi.org/10.1063/1.4817287

Published in:
Physics of Plasmas

Document Version:
Publisher's PDF, also known as Version of record

Laser-driven 1 GeV carbon ions from preheated diamond targets in the break-out afterburner regime

D. Jung, L. Yin, D. C. Gautier, H.-C. Wu, S. Letzring, B. Dromey, R. Shah, S. Palaniyappan, T. Shimada, R. P. Johnson, J. Schreiber, D. Habs, J. C. Fernández, B. M. Hegelich, and B. J. Albright

Citation: Physics of Plasmas **20**, 083103 (2013); doi: 10.1063/1.4817287
View online: http://dx.doi.org/10.1063/1.4817287
View Table of Contents: http://aip.scitation.org/toc/php/20/8
Published by the American Institute of Physics

Laser-driven 1 GeV carbon ions from preheated diamond targets in the break-out afterburner regime

D. Jung,[1,2,3,a)] L. Yin,[1] D. C. Gautier,[1] H.-C. Wu,[1] S. Letzring,[1] B. Dromey,[4] R. Shah,[1] S. Palaniyappan,[1] T. Shimada,[1] R. P. Johnson,[1] J. Schreiber,[2,3] D. Habs,[2,3] J. C. Fernández,[1] B. M. Hegelich,[1] and B. J. Albright[1]
[1]*Los Alamos National Laboratory, Los Alamos, New Mexico 87545, USA*
[2]*Department für Physik, Ludwig-Maximilians-Universität München, D-85748 Garching, Germany*
[3]*Max-Planck-Institut für Quantenoptik, D-85748 Garching, Germany*
[4]*Queen's University Belfast, Belfast BT7 1NN, United Kingdom*

(Received 19 February 2013; accepted 5 July 2013; published online 5 August 2013)

Experimental data are presented for laser-driven carbon C^{6+} ion-acceleration, verifying 2D-PIC studies for multi-species targets in the Break-Out Afterburner regime. With Trident's ultra-high contrast at relativistic intensities of 5×10^{20} W/cm^2 and nm-scale diamond targets, acceleration of carbon ions has been optimized by using target laser-preheating for removal of surface proton contaminants. Using a high-resolution wide angle spectrometer, carbon C^{6+} ion energies exceeding 1 GeV or 83 MeV/amu have been measured, which is a 40% increase in maximum ion energy over uncleaned targets. These results are consistent with kinetic plasma modeling and analytic theory. © *2013 AIP Publishing LLC*. [http://dx.doi.org/10.1063/1.4817287]

I. INTRODUCTION

For more than a decade, laser-driven ion acceleration has shown significant promise in fundamental as well as applied sciences. Progress has been made in the application of these ion sources to several settings, such as laser-driven proton radiography,[1] ion fast ignition (IFI),[2] and hadron cancer therapy.[3] Moreover, laser-driven ion beams have been used for the generation of secondary radiation sources, such as x-ray[4] and intense neutron beams.[5,6] Most common challenges for optimization and realization of these applications are conversion efficiency of laser into ion energy,[7,8] spectral beam control[9,10] and focusing,[11] and maximum ion energies.[12,13] The latter has received most of the research interest as ion energies remain too low for many applications. For carbon-FI, for instance, a (mono-energetic) beam of carbon C^{6+} ions with $E_k \approx 450$ MeV is necessary.[2] For the hadron cancer therapy protons of 250 MeV or carbon C^{6+} ions of 4–5 GeV are needed with a small energy spread.[14] With target normal sheath acceleration (TNSA),[15] protons have been accelerated to energies of 67 MeV[16] using laser intensities in excess of 10^{18} W/cm^2. In TNSA, electrons heated by the laser electric field at the front side of the target set up a virtual cathode on the back side of the target; there, protons from the surface hydro-contamination layer are dominantly accelerated by virtue of their highest charge to mass ratio. Additional techniques, such as target surface cleaning, enable acceleration of heavier ions, but maximum energies have not exceeded 10 MeV/amu.[17,18] These energies reduce the applicability of TNSA with present laser systems when requiring high-energy ions with $Z > 1$. With laser intensities exceeding 10^{20} W/cm^2 numerous alternative acceleration mechanisms are possible,[19] such as the radiation pressure acceleration (RPA),[20–22] the laser piston regime[23] or the Break-Out Afterburner (BOA).[24,25] These mechanisms have a common advantage: they efficiently transfer a large fraction of the laser energy into *all* target ions, in contrast to TNSA, where mostly surface atoms (hydro-contaminants in uncleaned targets) are accelerated. This advantage makes these mechanisms attractive to applications utilizing high-energy ions with $Z > 1$. However, acceleration dynamics of these novel mechanisms are much more influenced by the specific composition of the target, i.e., abundance of different ion species in the bulk of the target. For RPA and BOA, for instance, theoretical studies have shown that for a mixed target consisting of protons and carbon ions, the protons are accelerated to a quasi-monoenergetic beam.[20,21,24] Multi-species dynamics have not been investigated in detail in the BOA regime, though it has been shown that the BOA mechanism is robust to presence of contaminants through target "self-cleaning."[24]

Here, we present particle-in-cell (PIC) simulations and experimental data showing that multi-species dynamics govern maximum ion energies obtained in the BOA regime. In the simulations, we see that acceleration of carbon C^{6+} ions can be optimized by the removal of proton contamination, i.e., by using a pure carbon target. Experimentally, this was achieved by conventional CW laser-preheating and resulted in maximum carbon ion energies well in excess of 1 GeV (or >83 MeV/amu), an order of magnitude higher than achieved with TNSA and almost a factor of 2 higher than reported previously for experiments in the BOA regime.[7]

II. ION ACCELERATION IN THE BREAK-OUT AFTERBURNER REGIME

At the beginning of a high-intensity laser solid-matter interaction ($I > 10^{19}$ W/cm^2), the laser only interacts with the front surface as the penetration into the target is limited to the skin depth $l_s \propto c\sqrt{\gamma/n_e}$. With a linearly polarized

a)Electronic mail: daniel.jung@outlook.com

laser pulse, electrons at the front are heated in the laser field mostly due to $\vec{J} \times \vec{B}$ heating. When the thus created plasma starts to expand, the local electron density decreases and at the same time the electron γ_e further increases. As a result, the skin depth increases by a factor of $\sqrt{\gamma_e}$ and the laser evanescent field reaches deeper into the still opaque target, further enhancing hot electron generation. For targets of micron-scale thickness, acceleration of ions will be governed by TNSA as absorption of laser energy by the electrons will be confined to the front surface; preferentially, a beam of protons from surface impurities are accelerated normal to the front and back surface. Acceleration of ions in other regimes can be achieved with thinner targets of nm-thickness. (For these thicknesses, if the pedestal intensity is too high or prepulses are present, the target can suffer from premature ionization and subsequent destruction before the arrival of the peak pulse.) Provided sufficient laser contrast is available, laser penetration can encompass most or all of a nm-scaled target. If the target is still opaque at that time with $N/\gamma > 1$ and $N \equiv n_e/n_{cr}$, the normalized target electron density, acceleration via RPA or RPA light sail are possible. For that, circularly polarized laser light can be used to reduce $\vec{J} \times \vec{B}$ heating of the target. If, however, the target has turned relativistically transparent at the time the laser penetration has reached the end of the target with $N/\gamma \leq 1 < N$, conditions for BOA acceleration are met. The relativistic transparency is the most prominent characteristic of the BOA mechanism and also marks the boundary condition to where RPA cannot be operative anymore. Note that when the plasma reflectivity R has dropped to 0 (due to the self-induced relativistic transparency), the radiation pressure $P_r = 2IR/c$ vanishes[21] and momentum transfer via reflection of the laser becomes very inefficient. In BOA, on the other hand, the laser energy is dominantly transferred to the ions between time t_1, when the target becomes relativistically transparent, and time t_2, when peak target density relaxes to the classical critical density.[26] Before time t_1, acceleration of ions occurs in an electric field E_x determined by the distribution of hot electrons produced at the front side of the target. In simulations, ions only gain approximately 10% of their final kinetic energy during this time.[26] Between t_1 and t_2, when the target is relativistically transparent, electrons in the intense laser field are subject to a large forward drift with relativistic velocity. At the same time, ions are moving much slower. The resulting electron ion drift is known to be unstable to a kinetic Buneman instability,[27] which can efficiently couple electron momentum to ion momentum. In simulations, the relativistic electron drift drives such an instability, whose phase speed matches the drift speed of the ions and accelerates them resonantly.[25] In particular, the relativistic (electrostatic) Buneman reactive quasi-mode,[28] initially unstable, saturates by driving a compensating ion drift. This enables the transfer of forward momentum from the electrons to the ions; at the same time the laser can keep pushing on the electrons, increasing the mode phase speed, accelerating ions to higher energy. In that sense, the BOA mechanism is analogous to a traveling-wave conventional accelerator, or an electron wakefield accelerator. Optimal ion acceleration is obtained when peak laser intensity falls within this time window.

The problem of experimental validation is complicated, however, because one generally lacks measurements of the initial target conditions prior to the arrival of the main laser pulse and, therefore, is mostly limited to comparison of simulation output to integrated, indirect measurements. The dynamics of the relativistic transparency for BOA relevant laser and target parameters have recently been verified experimentally and published by Palaniyappan *et al.*[29] In an extensive experimental study, we also found that peak ion energies and conversion efficiency agrees well with PIC simulations.[7] Furthermore, from 3D-PIC simulations it has been found that highest energy carbon ions are emitted off-axis[30] (in contrast to TNSA or RPA, where peak ion energies are expected on-axis); this has been verified in recent experiments as well (see Ref. 12, a dedicated publication is currently being prepared).

III. SIMULATION METHODOLOGY AND CONVERGENCE STUDIES

The simulations employ the three-dimensional (3D), relativistic, electromagnetic, charge-conserving, PIC code VPIC[31] in a two-dimensional (2D) domain of 50 μm × 25 μm in the (x, z) plane (the target transverse width is 25 μm). The laser pulse is polarized along y, propagates along x, and has a time-varying intensity profile $I(t) = I_0 \sin^2(t\pi/\tau)$, where $I_0 = 5.2 \times 10^{20}$ W/cm^2 and $\tau/2 = 540$ fs is the FWHM. The central laser wavelength is 1054 nm, as in the experiments. The laser electric field has a 2D-Gaussian spatial profile with best focus at the target surface, where $E_y \sim \exp(-z^2/w^2)$ with $w = 5.12\,\mu$m, which is a good approximation of the experimental conditions described in Sec. V. For these laser parameters, the incident laser power in our simulations is $P(t) = 2\Delta y\, I_{\max}(t) \int_0^\infty \exp(-2r^2/w^2)\, dr = \sqrt{\pi/2}\Delta y\, w I_{\max}(t)$, where $I_{\max}$ is the laser intensity on axis and Δy is the spatial extent in the ignorable direction. Taking $\Delta y = w\sqrt{\pi/2}$ recovers $P(t) = (\pi/2) w^2 I_{\max}$, the power of a Gaussian beam in two transverse spatial dimensions. With this association, the incident laser energy is therefore $\mathcal{E} = \int dt\, P(t) = (\pi/4)\, \tau\, w^2 I_0 \sim 115$ J, which is comparable to the energy in the Trident experiments described later (80 J). Solid density C^{6+} (diamond like) targets at $n_e/n_{\rm cr} = 821$ (2.8 g/cm^3; $n_{\rm cr} = m_e\omega_0^2/4\pi e^2$ is the critical density in CGS units and ω_0 is the laser frequency) were employed both with and without 5% protons in number density. The density is initially a constant density slab profile. We use a target thickness of 58 nm, which was determined from prior thickness scaling studies using the same laser conditions[26] to recover the essential C ion acceleration dynamics in the BOA regime.

While the simulated target thickness of 58 nm was somewhat narrower than those employed in the experiments described later, they closely reproduced the maximum C ion energies. It is likely that this discrepancy in thickness can be accounted for by differences in capturing the dynamics in 2D and 3D (particularly the differences in the transverse ponderomotive expulsion of target plasma, which modifies the times t_1 and t_2). To retain the Debye length scale, the initial electron temperature is set to $T_e = 165$ keV; the ions are cold ($T_i = 10$ eV).

In experiments, one generally lacks measurements of the initial target conditions prior to the arrival of the main laser pulse and hydrodynamics simulations are unable to accurately predict the initial plasma conditions because the lack of proper flux-limiting models. In experiments when the main laser pulse interacts with the target, the target density profile is unlikely to be such an ideal slab profile because of the effects of finite laser prepulse. The finite laser prepulse in experiments could also lead to a somewhat lower peak target density when the main laser pulse interacts with the target; this may be another reason why the optimal target thickness from experiments is thicker than that from simulation. However, neither the specific shape of the initial density profile nor the particular target optimal thickness modifies the physics processes we describe in this paper.

The dynamics of laser propagation through dense targets and plasma expansion resulting from the finite electron temperature, which changes in time as the laser heats the electrons to relativistic energy, are the two important processes for modeling BOA. Kinetic simulation of laser interaction with highly overdense targets in higher-dimensions is challenging because of the requirement to spatially resolve the skin depth scale in order to accurately describe the laser propagation into the target and to retain Debye length scale in order to model dynamics, such as ion acoustic wave non-linearity at

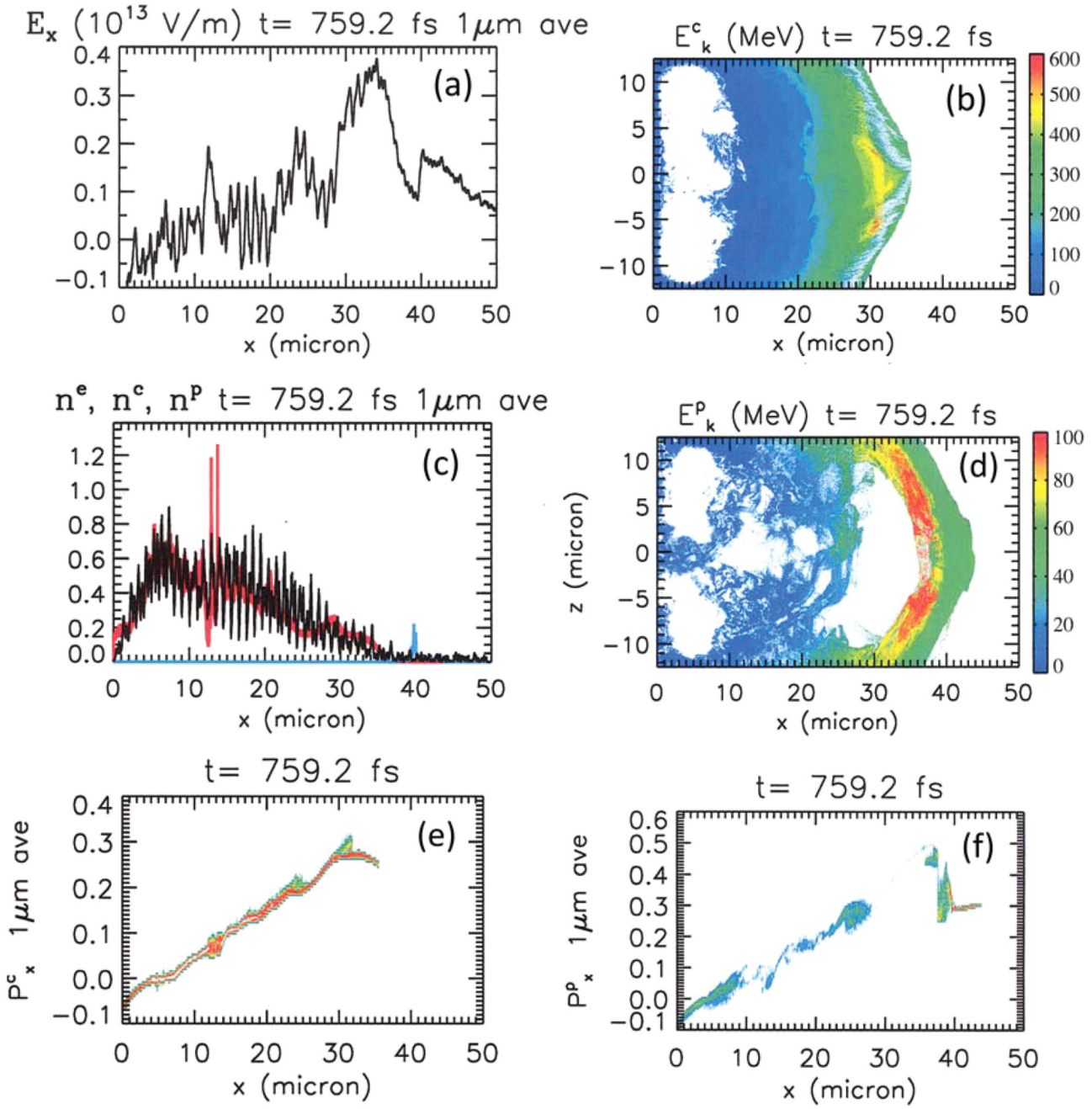

FIG. 1. 2D-VPIC simulation results (1 μm average over z) of a 58 nm diamond target with 5% protons at t = 759.2 fs when peak target density has classical critical density: (a) electric field E_x; (c) absolute value of charge density of electrons (n^e, black), C^{6+} ions (n^C, red), and proton (n^P, blue); (b) and (d) kinetic energy distribution of C^{6+} ions ($E^C{}_k$) and protons ($E^P{}_k$); (e) and (f) momentum phase space of C^{6+} ions ($P^C{}_x$) and protons ($P^O{}_x$). See text for details.

all times. In our simulations, the cell size was taken to be $\Delta x = 0.2c/\omega_{pe}^0$ ($\Delta z \sim 1c/\omega_{pe}^0$), i.e., 5 cells per skin depth required to accurately model the light wave propagation (not superfluously chosen), and $\Delta x = 0.35\lambda_D^0$ ($\Delta x = 1.76\lambda_D^0$) to accurately model the Debye length scale, given in terms of the plasma length scales at the initial time. We use 8210 particles per cell for each species.

Fig. 1 shows results from a simulation of diamond target with 5% protons (box length 50 μm) at the end of the acceleration when peak target density has relaxed to the classical critical density. All profiles shown are from a 1 μm average over z centered about the laser axis ($z = 0$). The profile of electric field E_x in (a) has a localized peak that accelerates the C^{6+} ions, whose x-component of momentum phase space and structure of the kinetic energy are shown in panels (b) and (e), respectively. A dense population of protons is seen to running ahead of the highest energy C^{6+} ions, as shown by the blue curve in (c) [which includes the absolute value of charge density of electrons (black) and C^{6+} ions (red)] as well as in (f) from the H^+ x-component of momentum phase space. The structure of the kinetic energy for H^+ is provided in panel (d).

The C^{6+} kinetic energy is given in Fig. 2 (blue solid line). In comparison, the red solid line shows results from a simulation of a diamond target without protons (same box length of 50 μm, spectrum taken at the end of the acceleration when peak target density has relaxed to the classical critical density, 1 μm average over z). The corresponding profiles of E_x and the x-component of momentum phase space characteristics for the pure diamond simulation are given in Figs. 3(a) and 3(b). Fig. 3(c) gives the C^{6+} kinetic energy (the black curve is from a 1 μm average over z along the laser axis while the red curve is averaged from the entire z-domain). Comparing both simulations, it is clear that without the protons, the highest C^{6+} energy has increased significantly, to ~1 GeV.

We have also examined the sensitivity of these dynamics to simulation box size. In Fig. 4, the simulation shown in Fig. 3 is repeated with a box length of 75 μm while the initial conditions and simulation resolution are kept the same. The localized E_x field, the C^{6+} x-component of momentum phase space, and the C^{6+} kinetic energy spectrum are found to be very similar to the results in Fig. 3 with maximum C^{6+} energy at ~1 GeV. Thus, it is reasonable to expect the results discussed in this work to be physical, unaffected by the simulation box length. (This is to be expected since the main BOA acceleration occurs predominantly within the narrow target layer—see the large, localized, longitudinal electric field in panels (a) in Figs. 3 and 4.)

Finally, we discuss some simulation sensitivity issues germane to this work. During the simulations, the plasma

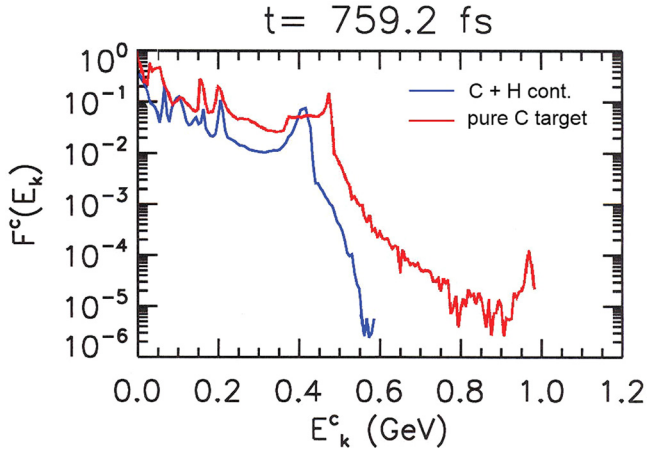

FIG. 2. Carbon C^{6+} spectra from 2D-VPIC simulation shown in Fig. 1 from a 58 nm diamond target mixed with 5% protons in number density (blue solid line) and a pure diamond target shown in Fig. 3 (red solid line); 1 μm average over z along the laser axis. Maximum carbon energies are 600 MeV and 1 Gev, respectively.

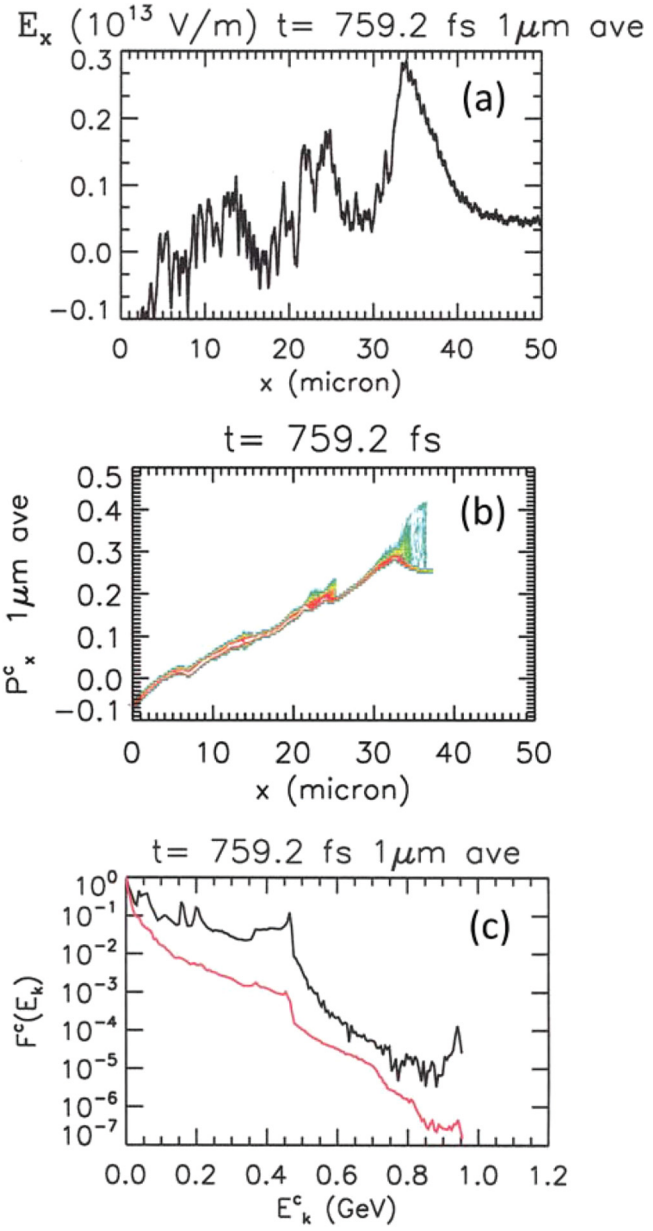

FIG. 3. 2D-VPIC simulation, same conditions as for simulation shown in Fig. 1, but using a diamond target without protons (box length of 50 μm, t = 759.2 fs at end of acceleration when peak target density has classical critical density, 1 μm average over z): (a) electric field E_x; (b) x-component of C^{6+} momentum phase space; (c) C^{6+} kinetic energy (black:1 μm average, red: entire z-domain).

Finally, we discuss some simulation sensitivity issues germane to this work. During the simulations, the plasma

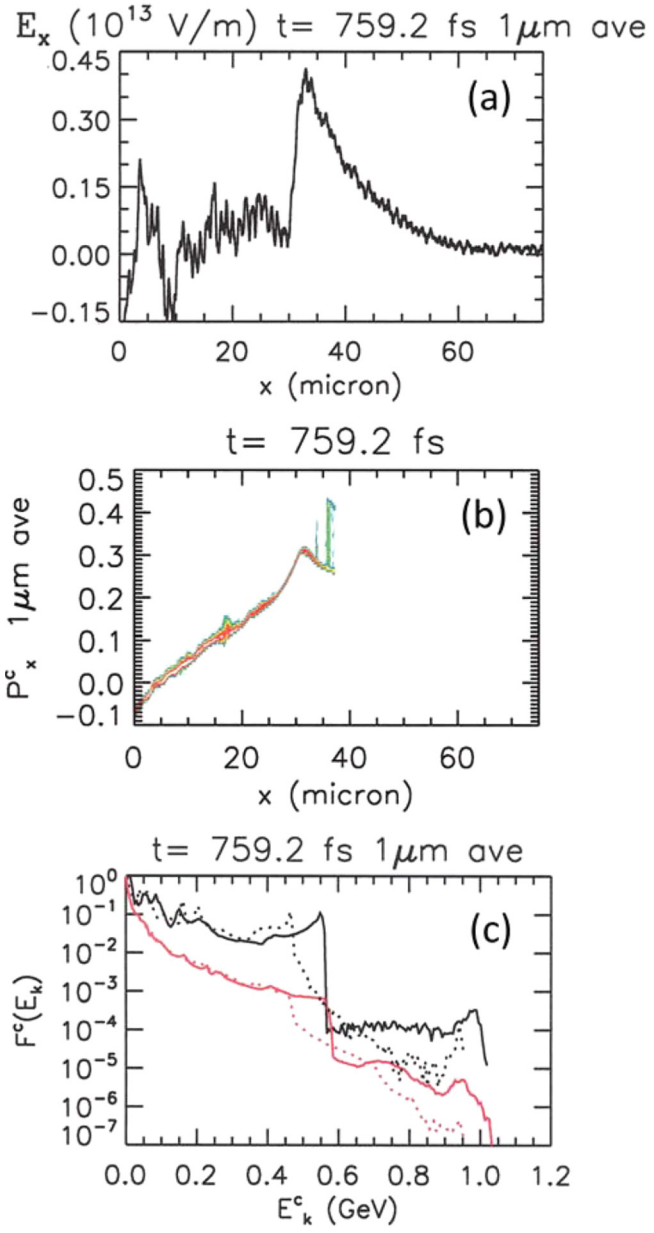

FIG. 4. 2D-VPIC simulation, same conditions as for simulation shown in Fig. 3, but using a box length of 75 μm. Plots are at t = 759.2 fs, the end of acceleration when peak target density has classical critical density and from a 1 μm average over z: (a) electric field E_x; (b) x-component of C^{6+} momentum phase space; (c) C^{6+} kinetic energy (solid black:1 μm average, solid red: entire z-domain, dotted lines are results from Fig. 3 with a simulation box of 50 μm).

density decreases, the skin depth $\delta_e = \sqrt{c^2 m_e \gamma / 4\pi e^2 n_e}$ and the Debye length increase as the electron temperature increases. Thus, the initial spatial resolution meets the requirements for properly resolving the light wave propagation and ion sound wave nonlinear dynamics throughout the simulation.

The number of particles in a "Debye square," a square with side of length the Debye length, is also sufficient in our simulations to faithfully represent the dynamics without significant deviations resulting from finite-particle-number statistics: We use 8210 particles per cell initially; at a later time when $n_e = 20 n_{cr}$ (for example, when the target becomes transparent), the simulation still has 200 particles/cell within the target, which implies that within a Debye square we have 1.6 million computational electron macro-particles per species, thus providing a good statistical representation of a collisionless plasma. At the end of the BOA main acceleration phase, when $n_e \approx n_{cr}$, the number of particles per cell decreases to ~10, but we still have more than 1.6 million particles/Debye square ($T_e > 20$ MeV at this time, so the Debye length is yet larger than the above). Based on this analysis and particle-number convergence studies conducted in the past, in our simulations, the physically meaningful spatial scales indeed appear to be resolved well throughout the simulation. We have further examined the sensitivity of the dynamics to the initial electron temperature used in BOA simulations. In Fig. 7(a) of Ref. 26, three values of initial T_e are used: 10 eV, 18 keV, and 165 keV. For the $T_e = 165$ keV simulation, the spatial resolution is the same as described above and the Debye length scale is retained; for $T_e = 18$ keV, $\Delta x \sim 0.05 c/\omega_{pe}^0 = 0.3\lambda_D^0$, $\Delta z = \sim 0.3 c/\omega_{pe}^0 = 1.7\lambda_D^0$, and the Debye length scale is also retained. On the other hand, for $T_e = 10$ eV, $\Delta x = 45\lambda_D^0$, and $\Delta z = 226\lambda_D^0$, so the Debye length scale is not retained; γ^e can increase in the laser field at the front surface through $\vec{j} \times \vec{B}$ heating, but the bulk electron temperature does not increase appreciably in the absence of binary collisions in the PIC code. Consequently, ion sound wave propagation (and thus rarefaction wave propagation across the target and, consequently, target expansion) will be inadequately modeled, whereas the target will continue to be compressed by the laser pressure at the front target surface. Thus, the use of such resolution will lengthen artificially the time interval required for transparency to occur. Comparison of the results from these two simulations shows that the overall effect of initial electron temperature on the ion acceleration is small, provided the Debye length scale is retained, whereas the ion energy obtained is significantly different in the $T_e = 10$ eV case, thus casting doubt on simulations that do not resolve the structure of the plasma. At the present time, because of limitations of computing power, modeling laser interaction with solid density targets using *ab initio* kinetic simulations require that the modeler make a choice to either retain the Debye length scale by the use of a higher initial electron temperature (as done in this work) or by using initially cold plasma and neglecting physics that occur on such scales. Unfortunately, these two choices can lead to much different dynamics and, worse, processes, such as the BOA, that rely upon capturing the internal structure of the targets may be missed by the practice of under-resolving one's simulations.

For completeness, as commented upon above, we note that we have also examined the sensitivity of our results to the number of macro-particles per computational cell, which might be expected to affect the simulated dynamics at the very ends of our simulations, as the target density drops to $n_e \approx n_{cr}$. Fig. 7(b) of Ref. 26 indicates results of carbon spectra from 27 nm target simulations using 500 (black curve), 8210 (green), and 16420 (red) particles per cell for each species, compared at time when $n_e \approx n_{cr}$. We find that the 500 particle per cell simulations tend to over-estimate somewhat the maximum ion energy. This is because

although the skin depth and Debye length scales are still well resolved, the 500 particle per cell simulation has when $n_e \approx n_{cr}$ fewer than one particle/cell on average, so the accumulation of particle charge density or electrical current onto the grids exhibits $\mathcal{O}(1)$ statistical fluctuations that appear to upscatter in energy some of the fastest carbon ions, as reflected in the maximum energy in the ion spectrum (in the black curve).

IV. SIMPLE KINEMATIC MODEL OF PROTON INERTIAL TAMPING OF CARBON IONS

As seen in kinetic simulations and in experiments, as will be shown later, removal of protons from diamond targets leads to a substantial increase in peak carbon energy. How this occurs can be understood from a simple model of inertial tamping of the fastest carbon ions by the protons. In the kinetic simulations, the protons (when present) readily outrun the C in the early phases of the acceleration, a type of target "self-cleaning" that proceeds during the early TNSA phase of the BOA prior to the onset of relativistic transparency.[24] During this early phase, the protons acquire relatively low kinetic energy.

Then, relativistic transparency occurs in the main target target layer containing carbon ions and the bulk of the electrons. During this acceleration, much larger electrostatic fields are present inside the target that is able to accelerate the carbon ions into the protons. However, the carbon ions are seen both in these and prior simulations[24] to be unable to outrun the protons, the latter behaving much like a Lagrangian fluid that accelerates out in front of the carbon ions. The fastest carbon ions decelerate, "piling up" against the proton layer (when present) and the protons accelerate to the same speed as these piled-up carbon ions. Throughout the remainder of the acceleration, the protons, by virtue of their higher charge-to-mass ratios, remain in front of the carbon ions. This process proceeds much like an inertial tamping of the fastest carbon ions by the protons.

We may estimate the role of the protons in this tamping by balancing the momentum acquired by the protons with that lost by the fastest carbon ions, thus determining the dependence of the cutoff energy E_{cut} of the carbon ions on the relative proton number fraction within the target. Let us assume that in the absence of protons, the carbon ions would obtain a Boltzmann-like energy spectrum $f_C(E) \approx (N_C/T_C)\exp(-E/T_C)$, where N_C is the number of carbon ions in the spectrum and T_C is their characteristic temperature. Consider the population of carbon ions with energy $E > E_{cut} \gg T_C$. These ions have momentum

$$p_> = \int_{E_{cut}}^{\infty} dE f_C(E)\sqrt{2m_C E} = N_C\left[\sqrt{2m_C E_{cut}}\exp\left(-\frac{E_{cut}}{T_C}\right) + \sqrt{\frac{\pi m_C T_C}{2}}\mathrm{erfc}\left(\sqrt{\frac{E_{cut}}{T_C}}\right)\right], \quad (1)$$

where erfc is the complimentary error function.[32] In the presence of protons, these ions would be tamped. We model this by assuming that this population of ions is slowed to energy E_{cut} with corresponding momentum

$$p_{cut} = \int_{E_{cut}}^{\infty} dE f_C(E)\sqrt{2m_C E_{cut}} = N_C\left[\sqrt{2m_C E_{cut}}\exp\left(-\frac{E_{cut}}{T_C}\right)\right]. \quad (2)$$

Subtracting the two momenta yields the net momentum lost by the fastest carbon ions through tamping

$$\Delta p_C = N_C\sqrt{\frac{\pi m_C T_C}{2}}\mathrm{erfc}\left(\sqrt{\frac{E_{cut}}{T_C}}\right) \sim N_C T_C\sqrt{\frac{m_C}{2E_{cut}}}\exp\left(-\frac{E_{cut}}{T_C}\right). \quad (3)$$

We ignore momentum going into the electrons and equate this momentum lost by carbon ions with that gained by the protons. For simplicity, let us assume that the protons acquire negligible momentum during their initial, TNSA expansion and that they accelerate as a cold blob up to the same speed as carbon ions at energy E_{cut}, so their momentum gain will be

$$\Delta p_H = m_H N_H\sqrt{\frac{2E_{cut}}{m_C}}. \quad (4)$$

Equating Δp_H with Δp_C and defining the total mass ratio of ions in target $\Phi \equiv m_C N_C/m_H N_H$, we obtain a transcendental relation for E_{cut}/T_C

$$\frac{E_{cut}}{T_C} = \frac{\Phi}{2}\exp\left(-\frac{E_{cut}}{T_C}\right) \quad (5)$$

that may be iterated numerically or approximated when $\Phi \gg 1$ (specifically, $\Phi > 5.44$) to yield, simply,

$$\frac{E_{cut}}{T_C} \approx \log\left(\frac{\Phi}{2}\right) - \log\log\left(\frac{\Phi}{2}\right). \quad (6)$$

The leading-order logarithmic dependence of the cutoff energy on the mass ratio Φ indicates that even a small population of protons can significantly lower the maximum carbon ion cutoff energy, as observed in our experiments and simulations.

As a final point, while we freely admit that this kinematic model is simplistic and neglects potentially important physics (e.g., non-Boltzmann energy distributions of carbon ions, momentum gained by protons prior to relativistic transparency, and three-dimensional effects on the tamping process), one could, in principle, treat these tamping dynamics more completely by incorporating, e.g., a Poisson solve of the nonlinear electron/multi-component ion system such as has been reported elsewhere for multi-component TNSA targets.[34] (While these TNSA results bear superficial resemblance to this problem, the two systems are, in fact, distinct—these other models examine expansion of a light-ion layer away from the adjoining heavy ion layer in a TNSA

sheath, whereas in our case, owing to the different acceleration dynamics of the BOA, the heavy ions are accelerated into the light ions, thus leading to different dynamics.)

V. EXPERIMENTAL REALIZATION

We have validated the simulation results for these mixed target dynamics at the Trident laser facility;[35] the laser has 80 J in ~550 fs at a wavelength of 1054 nm and linear s-polarization. An F/3 off-axis parabolic mirror yields a measured on-target focus of ~6 μm radius ($1/e^2$-condition, containing >60% of the laser energy) and a peak intensity 5×10^{20} W/cm^2, closely matching the simulation parameters. The Trident laser comprises an exceedingly high contrast level without use of plasma mirrors by employing an Optical Parametric Amplification Prepulse Eliminator (OPAPE)[36] (measured on target at full energy, single-shot, to be 10^{-7} at −4 ps) that allows overdense interaction with targets as thin as 5 nm.[37] The laser was normally incident on synthetically grown diamond foil targets.[38] Untreated, diamond targets typically have a nm-thick hydro-contamination layer on each side.

From previous experiments, the optimum thickness for acceleration in the BOA regime has been found to be about 200 nm (see Ref. 7 for a full thickness scan). The difference in the optimum thickness for the simulation and the experiment mainly arises from the imperfect laser contrast. The preceding pedestal of the laser pulse (which is not accounted for in the simulation) heats the target prior to the arrival of the peak pulse, causing premature target expansion and decrease in the initial electron density; thus, the optimum target for BOA is slightly thicker in the experiment.

Angularly resolved C^{6+} spectra were measured from −2.5° to 22.5° with respect to laser and target normal in a plane either parallel or perpendicular to the laser polarization axis using the ion wide angle spectrometer (iWASP). The iWASP is based on a magnetic field perpendicular to the ion propagation direction and introduces an energy dependent dispersion of the particle beam. A long slit, about 2 cm behind the target, is positioned parallel to and in front of the magnetic field so that the energy distribution of the source ions is angularly resolved in the dimension along the slit. The experimental setup is identical to Fig. 1 in Ref. 33. The axis going through the laser spot center corresponds to 0° in the spectrum. The iWASP has a low-energy cutoff of 33 MeV (given by 32 μm of Al filtering in front of the nuclear track detector (CR39)[39]). In this setup, the iWASP has a solid angle of 0.4 msr, 3–5 orders of magnitude higher than conventional Thomson parabolas.[9,40] This ensures a significantly increased accuracy in the measured maximum energies, as a much larger fraction of the beam is analyzed and the flux-based high-energy detection threshold is increased.

It should also be noted that the iWASP lacks charge separation of a Thomson parabola. While protons, due to their much lower stopping power and size are not visible on the CR39, unless etched for hours, lower charge states of carbon (such as C^{5+} or C^{4+}) can potentially contaminate the C^{6+} signal on the CR39. However for the optimum BOA target

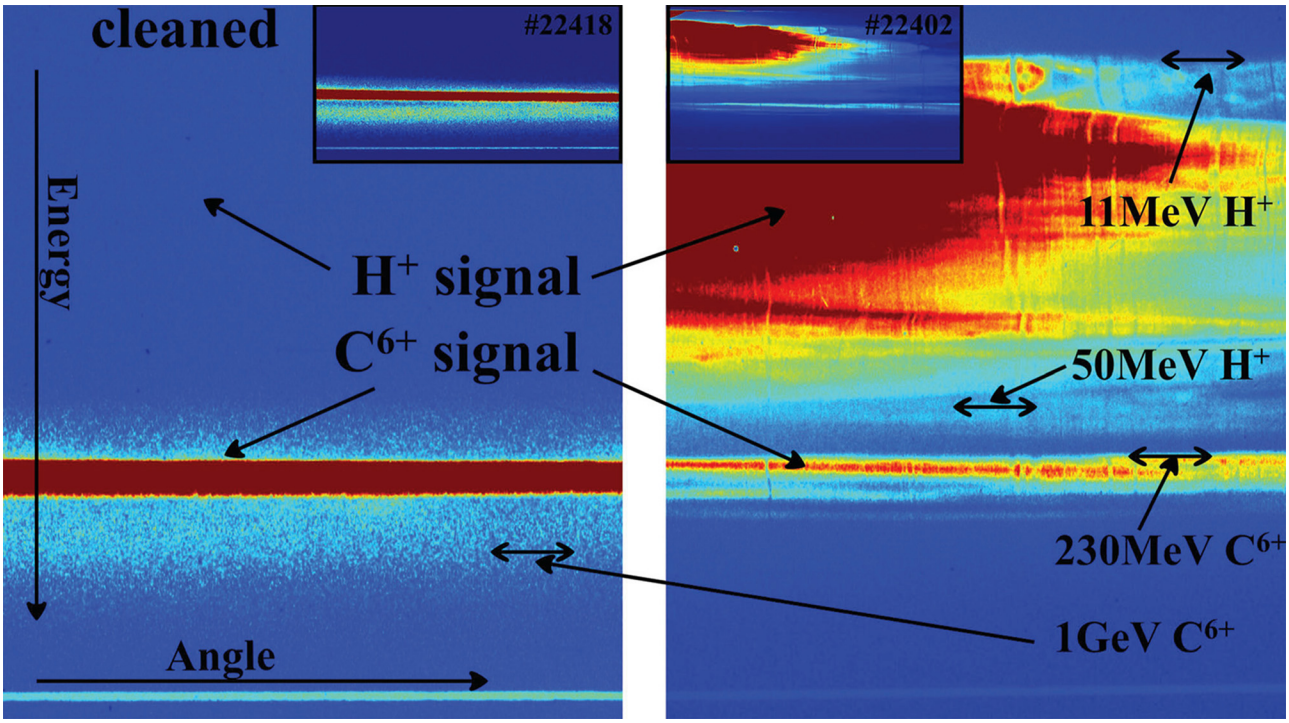

FIG. 5. Raw IP data from the ion wide angle spectrometer for a heated (cleaned) diamond target (left) and an unheated diamond target (right), both with thickness 225 nm. The IP shows protons and ions with energy high enough to pass the filtering in front of the IP (>11 MeV for H^+ and >230 MeV for C^{6+}). Energy increases from top to bottom, some energies are given as a guide for the eye; angle is from left to right; flux is color coded with blue = none to red = high. While the right image shows a strong proton distribution for the unheated target, the left image is devoid of any protons. In the lower portion of the image, a carbon distribution is visible for both targets; however, the one for the cleaned target extends to much higher energies. Note that the raw IP signal is a convolution of the IP response, the ion stopping power and the filtering; see Ref. 33 for a detailed explanation of the raw data.

thickness, the abundance of C^{6+} is very high (typically >90%[7,33]). In addition, lower charged carbon ions experience less acceleration due to their lower charge to mass ratio and will only contaminate the low energy tail of the spectrum, which is not of interest here.

In order to realize a pure carbon target, we employed laser-heating of the target with a 3 W, 532 nm Verdi laser,[41] and an on-target focus of ~100 μm in radius. Note that although this technique has been used in the TNSA regime,[42] the impact on the acceleration dynamics and the underlying physics are fundamentally different. In TNSA, cleaning changes the main species being accelerated, i.e., with cleaning, carbon ions are accelerated instead of protons from a diamond target. Here, the main species being accelerated is unchanged; instead, acceleration dynamics are modified, as explained before.

The effectiveness of the target cleaning can be seen in Fig. 5, where raw image plate (IP) data from the iWASP are shown for a cleaned (left) and unheated target (right) near the optimum target thickness of 225 nm. The IP data show protons and carbon ions with energies sufficiently high to pass the 32 μm Al-shielding and the 1 mm thick CR39 in front of it; for protons this corresponds to energies above 11 MeV and for carbon ions above 230 MeV. Energy increases from the top to the bottom of the image; the solid line above the arrow marked with "Angle" is the zeroth order of the spectrometer, i.e., the projection of the spectrometer entrance slit (see figure caption and Ref. 37 for more details). Compared with the uncleaned target, the heated target is completely devoid of protons and much higher carbon C^{6+} energies are measured.

In Fig. 6, C^{6+} spectra are shown in absolute numbers; the spectra are obtained from the CR39 nuclear track detector in front of the IP for the same shots as shown in Fig. 5. For the unheated diamond target (blue solid line), i.e., the target with hydro-carbon contamination, a maximum carbon energy of (600 ± 35) MeV (or ~50 MeV/amu) has been measured. In fact, in over 100 shots, carbon energies never exceeded 700 MeV for unheated targets (see thickness scan in Ref. 7). For the heated and cleaned pure diamond target, the spectrum has a high-energy cutoff at (1050 ± 80) MeV, almost a factor of 2 greater than for the unheated target and in reasonable agreement with the simulations. Particle numbers for ions with kinetic energy above 900 MeV are $\sim 5 \times 10^4$/msr, measured over a solid angle of 0.4 msr with the iWASP. With the ion beam covering approximately 400 msr,[7] absolute numbers above this energy can be estimated to be on the order of 10^7, containing about 3 mJ. For energies from 400 MeV to 500 MeV, relevant to carbon-FI, the unheated target gives 1.1×10^5/msr, the cleaned target yields 2.5×10^5/msr. Although not mono-energetic, this is a factor of 2 more particles, or a doubled conversion efficiency of laser energy into carbon ions relevant to IFI. If successfully combined with the ion-soliton technique described in Refs. 37 and 43, this could mark a breakthrough for carbon-FI.

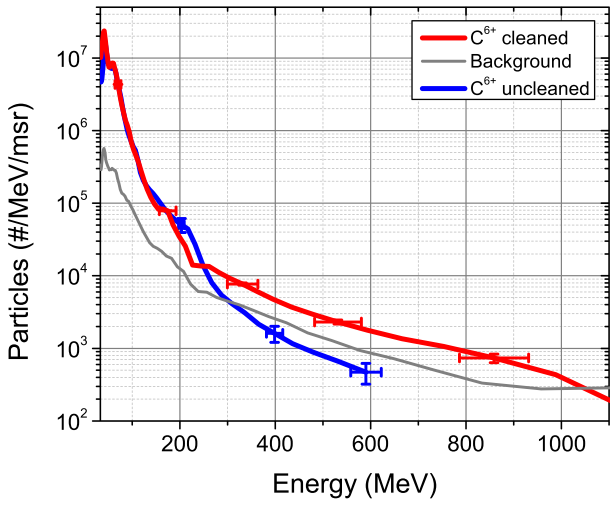

FIG. 6. Carbon C^{6+} spectra extracted from CR39 nuclear track detector in front of the IP in the ion wide angle spectrometer for an unheated 225 nm target (blue solid line) and a pre-heated 225 nm target (red solid line), i.e., without hydro-carbon surface contamination. The background for the heated spectrum is given by the grey solid line; the spectrum for the uncleaned target hast the background already subtracted. Maximum energies are (600 ± 32) MeV and (1050 ± 75) MeV, respectively. Error bars represent minimum instrument error. The spectrum is an average from 4° to 6° of the angularly resolved spectrum that covers −2° to 20° with respect to the laser propagation direction and orthogonal to the laser polarization plane.

VI. CONCLUSIONS

In conclusion, we presented a VPIC analysis of the influence of mixed targets on laser-driven acceleration in the BOA regime and found that the target mixture has a strong influence on the maximum ion energies, in agreement with a simple momentum conservation argument. For a diamond target contaminated with a hydro-carbon surface layer, carbon ions are tamped by a layer of proton contaminants, which comprise a natural barrier for the fastest carbon ions. The experimental results are in reasonable agreement with simulations. If we remove the proton contamination of the target by laser-preheating, we optimize acceleration of carbon ions in the BOA regime and achieve nearly a factor of 2 higher maximum energies (with up to 1050 MeV) and laser conversion efficiency into fast ions. The technique should furthermore be transferable to any species. For optimization of proton acceleration in the BOA regime, a pure hydrogen target should be used. The tamping of the carbon species by the preceding proton population could also be used to shape the resulting carbon energy spectrum. These are important steps toward realization of ion beams suitable for applications, such as proton and carbon ion cancer treatment, where extreme energies of 250 MeV and 4 GeV are required, respectively.

ACKNOWLEDGMENTS

We are grateful for the support of the Trident laser team in conducting the experiments. The simulations were run on the LANL ASC Roadrunner and Cielo supercomputers. Work was supported by DOE OFES, Deutsche Forschungsgemeinschaft (DFG) through Transregio SFB TR18, DFG Cluster of Excellence Munich-Center for Advanced Photonics (MAP), and DFG LMU-Excellence. Work performed under the auspices of the U.S. Department of Energy by the Los Alamos National Security, LLC, Los Alamos National Laboratory.

[1]J. A. Cobble, R. P. Johnson, T. E. Cowan, N. R.-L. Galloudec, and M. Allen, J. Appl. Phys. **92**, 1775 (2002).
[2]J. C. Fernández, J. Honrubia, B. J. Albright, K. A. Flippo, D. C. Gautier, B. M. Hegelich, M. J. Schmitt, M. Temporal, and L. Yin, Nucl. Fusion **49**, 065004 (2009).
[3]S. Bulanov, T. Esirkepov, V. Khoroshkov, A. Kuznetsov, and F. Pegoraro, Phys. Lett. A **299**, 240 (2002).
[4]A. B. Sefkow, G. R. Bennett, M. Geissel, M. Schollmeier, B. C. Franke, and B. W. Atherton, Phys. Rev. Lett. **106**, 235002 (2011).
[5]D. P. Higginson, J. M. McNaney, D. C. Swift, G. M. Petrov, J. Davis, J. A. Frenje, L. C. Jarrott, R. Kodama, K. L. Lancaster, A. J. Mackinnon, H. Nakamura, P. K. Patel, G. Tynan, and F. N. Beg, Phys. Plasmas **18**, 100703 (2011).
[6]M. Roth, D. Jung, K. Falk, N. Guler, O. Deppert, M. Devlin, A. Favalli, J. Fernandez, D. Gautier, M. Geissel, R. Haight, C. E. Hamilton, B. M. Hegelich, R. P. Johnson, F. Merrill, G. Schaumann, K. Schoenberg, M. Schollmeier, T. Shimada, T. Taddeucci, J. L. Tybo, F. Wagner, S. A. Wender, C. H. Wilde, and G. A. Wurden, Phys. Rev. Lett. **110**, 044802 (2013).
[7]D. Jung, L. Yin, B. J. Albright, D. C. Gautier, S. Letzring, B. Dromey, M. Yeung, R. Hörlein, R. Shah, S. Palaniyappan, K. Allinger, J. Schreiber, K. J. Bowers, H.-C. Wu, J. C. Fernandez, D. Habs, and B. M. Hegelich, New J. Phys. **15**, 023007 (2013).
[8]D. S. Hey, M. E. Foord, M. H. Key, S. L. LePape, A. J. Mackinnon, P. K. Patel, Y. Ping, K. U. Akli, R. B. Stephens, T. Bartal, F. N. Beg, R. Fedosejevs, H. Friesen, H. F. Tiedje, and Y. Y. Tsui, Phys. Plasmas **16**, 123108 (2009).
[9]D. Jung, R. Horlein, D. Kiefer, S. Letzring, D. C. Gautier, U. Schramm, C. Hubsch, R. Ohm, B. J. Albright, J. C. Fernandez, D. Habs, and B. M. Hegelich, Rev. Sci. Instrum. **82**, 013306 (2011).
[10]C. A. J. Palmer, N. P. Dover, I. Pogorelsky, M. Babzien, G. I. Dudnikova, M. Ispiriyan, M. N. Polyanskiy, J. Schreiber, P. Shkolnikov, V. Yakimenko, and Z. Najmudin, Phys. Rev. Lett. **106**, 014801 (2011).
[11]M. Schollmeier, S. Becker, M. Geißel, K. A. Flippo, A. Blažević, S. A. Gaillard, D. C. Gautier, F. Grüner, K. Harres, M. Kimmel, F. Nürnberg, P. Rambo, U. Schramm, J. Schreiber, J. Schütrumpf, J. Schwarz, N. A. Tahir, B. Atherton, D. Habs, B. M. Hegelich, and M. Roth, Phys. Rev. Lett. **101**, 055004 (2008).
[12]B. Hegelich, D. Jung, B. Albright, J. Fernandez, D. Gautier, C. Huang, T. Kwan, S. Letzring, S. Palaniyappan, R. Shah, H.-C. Wu, L. Yin, A. Henig, R. Hörlein, D. Kiefer, J. Schreiber, X. Yan, T. Tajima, D. Habs, B. Dromey, and J. Honrubia, Nucl. Fusion **51**, 083011 (2011).
[13]S. V. Bulanov, E. Y. Echkina, T. Z. Esirkepov, I. N. Inovenkov, M. Kando, F. Pegoraro, and G. Korn, Phys. Plasmas **17**, 063102 (2010).
[14]T. Tajima, D. Habs, and X. Yan, Rev. Accel. Sci. Technol. **2**, 201 (2009).
[15]S. P. Hatchett, C. G. Brown, T. E. Cowan, E. A. Henry, J. S. Johnson, M. H. Key, J. A. Koch, A. B. Langdon, B. F. Lasinski, R. W. Lee, A. J. Mackinnon, D. M. Pennington, M. D. Perry, T. W. Phillips, M. Roth, T. C. Sangster, M. S. Singh, R. A. Snavely, M. A. Stoyer, S. C. Wilks, and K. Yasuike, Phys. Plasmas **7**, 2076 (2000).
[16]S. A. Gaillard, T. Kluge, K. A. Flippo, M. Bussmann, B. Gall, T. Lockard, M. Geissel, D. T. Offermann, M. Schollmeier, Y. Sentoku, and T. E. Cowan, Phys. Plasmas **18**, 056710 (2011).
[17]J. Fuchs, P. Antici, E. d'Humieres, E. Lefebvre, M. Borghesi, E. Brambrink, C. A. Cecchetti, M. Kaluza, V. Malka, M. Manclossi, S. Meyroneinc, P. Mora, J. Schreiber, T. Toncian, H. Pepin, and P. Audebert, Nat. Phys. **2**, 48 (2006).
[18]M. Hegelich, S. Karsch, G. Pretzler, D. Habs, K. Witte, W. Guenther, M. Allen, A. Blazevic, J. Fuchs, J. C. Gauthier, M. Geissel, P. Audebert, T. Cowan, and M. Roth, Phys. Rev. Lett. **89**, 085002 (2002).
[19]G. Petrov and J. Davis, Appl. Phys. B **96**, 773 (2009).
[20]O. Klimo, J. Psikal, J. Limpouch, and V. T. Tikhonchuk, Phys. Rev. ST Accel. Beams **11**, 031301 (2008).
[21]A. Macchi, S. Veghini, T. V. Liseykina, and F. Pegoraro, New J. Phys. **12**, 045013 (2010).
[22]B. Aurand, S. Kuschel, O. Jäckel, C. Rödel, H. Y. Zhao, S. Herzer, A. E. Paz, J. Bierbach, J. Polz, B. Elkin, G. G. Paulus, A. Karmakar, P. Gibbon, T. Kuehl, and M. C. Kaluza, N. J. Phys. **15**, 033031 (2013).
[23]T. Esirkepov, M. Borghesi, S. V. Bulanov, G. Mourou, and T. Tajima, Phys. Rev. Lett. **92**, 175003 (2004).
[24]L. Yin, B. J. Albright, B. M. Hegelich, K. J. Bowers, K. A. Flippo, T. J. T. Kwan, and J. C. Fernandez, Phys. Plasmas **14**, 056706 (2007).
[25]B. J. Albright, L. Yin, K. J. Bowers, B. M. Hegelich, K. A. Flippo, T. J. T. Kwan, and J. C. Fernandez, Phys. Plasmas **14**, 094502 (2007).
[26]L. Yin, B. J. Albright, D. Jung, R. C. Shah, S. Palaniyappan, K. J. Bowers, A. Henig, J. C. Fernndez, and B. M. Hegelich, Phys. Plasmas **18**, 063103 (2011).
[27]O. Buneman, Phys. Rev. **115**, 503 (1959).
[28]D. B. Melrose, J. Plasma Phys. **36**, 269 (1986).
[29]S. Palaniyappan, B. M. Hegelich, H.-C. Wu, D. Jung, D. C. Gautier, L. Yin, B. J. Albright, R. P. Johnson, T. Shimada, S. Letzring, D. T. Offermann, J. Ren, C. Huang, R. Hörlein, B. Dromey, J. C. Fernandez, and R. C. Shah, Nat. Phys. **8**, 763 (2012).
[30]L. Yin, B. J. Albright, K. J. Bowers, D. Jung, J. C. Fernández, and B. M. Hegelich, Phys. Rev. Lett. **107**, 045003 (2011).
[31]K. J. Bowers, B. J. Albright, L. Yin, B. Bergen, and T. J. T. Kwan, Phys. Plasmas **15**, 055703 (2008).
[32]M. Abramowitz and I. A. Stegun, *Handbook of Mathematical Functions* (United States Department of Commerce, 1964), p. 297.
[33]D. Jung, R. Hörlein, D. C. Gautier, S. Letzring, D. Kiefer, K. Allinger, B. J. Albright, R. Shah, S. Palaniyappan, L. Yin, J. C. Fernández, D. Habs, and B. M. Hegelich, Rev. Sci. Instrum. **82**, 043301 (2011).
[34]B. J. Albright, L. Yin, B. M. Hegelich, K. J. Bowers, T. J. T. Kwan, and J. C. Fernández, Phys. Rev. Lett. **97**, 115002 (2006).
[35]J. Workman, J. Cobble, K. Flippo, D. C. Gautier, and S. Letzring, Rev. Sci. Instrum. **79**, 10E905 (2008).
[36]R. C. Shah, R. P. Johnson, T. Shimada, K. A. Flippo, J. C. Fernandez, and B. M. Hegelich, Opt. Lett. **34**, 2273 (2009).
[37]D. Jung, L. Yin, B. J. Albright, D. C. Gautier, R. Hörlein, D. Kiefer, A. Henig, R. Johnson, S. Letzring, S. Palaniyappan, R. Shah, T. Shimada, X. Q. Yan, K. J. Bowers, T. Tajima, J. C. Fernández, D. Habs, and B. M. Hegelich, Phys. Rev. Lett. **107**, 115002 (2011).
[38]See http://www.usappliedddiamond.com for information about Applied Diamond, Inc., manufacturers of the CVD targets used in this experiment.
[39]R. L. Fleischer, P. B. Price, and R. M. Walker, J. Appl. Phys. **36**, 3645 (1965).
[40]J. J. Thomson, Philos. Mag. Ser. 6 **22**, 469 (1911).
[41]See http://www.coherent.com for information about Coherent, manufacturers of the probe laser used in this experiment.
[42]B. M. Hegelich, B. J. Albright, J. Cobble, K. Flippo, S. Letzring, M. Paffett, H. Ruhl, J. Schreiber, R. K. Schulze, and J. C. Fernández, Nature **439**, 441 (2006).
[43]L. Yin, B. J. Albright, D. Jung, K. J. Bowers, R. C. Shah, S. Palaniyappan, J. C. Fernandez, and B. M. Hegelich, Phys. Plasmas **18**, 053103 (2011).